MEMS Resonator Synthesis for Testability

Nilmoni Deb, Sitaraman V. Iyer, Tamal Mukherjee and R. D. (Shawn) Blanton
ECE Department
{ndeb, sita, tamal, blanton}@ece.cmu.edu
Carnegie Mellon University
Pittsburgh, PA 15213-3890

ABSTRACT

We combine our MEMS synthesis and test capabilities into a synthesis-for-test environment. A microresonator design meeting a variety of specifications is synthesized. The susceptibility of this design is then measured using our MEMS contamination analyzer. The nature of each defective microresonator is determined and the deviation from nominal performance is correlated to the bounds and design constraints used in the synthesis process. Feedback from this analysis is formulated into additional design constraints for the synthesis tool with the object of minimizing the impact of spot contaminations. Re-synthesis of the same designs using these additional constraints indicates that a certain class of catastrophic and parametric faults can be reduced by 25% without sacrificing performance.

1 INTRODUCTION

Microelectromechanical Systems (MEMS) has existed as a technical field since the early 1980s. Past research has primarily focused on developing new process technologies to support specific applications. As stable process technologies have emerged, many research efforts have shifted towards the design of systems containing hundreds or even thousands of mixed-domain components. As a result, there is a growing need for CAD tools that shorten the design and development time for MEMS-based products. Success in this area depends greatly on new design methods that allow complex microsystems of mechanical, electrical, thermal, fluidic, and optical components to be hierarchically designed and integrated. MEMS layout synthesis allows rapid layout generation from engineering performance specifications to enable hierarchical design. In addition, CAD tools capable of assessing and preventing faulty MEMS behavior are also necessary to ensure the end quality of complex MEMS-based products. Here, we describe the integration of our MEMS synthesis and test tools to meet the functional and test objective through synthesis. The device used in this exercise is the surface-micromachined, folded-flexure, electrostatic comb-drive micromechanical resonator introduced by Tang et al. [1].

Surface-micromachined MEMS are a class of MEMS devices where the micromechanical structure is fabricated using layers of thin films deposited on the substrate. Surface micromachining enables the fabrication of high-quality sensors and actuators as MEMS devices. Most commercial applications use surface micromachining because of its well-developed infrastructure for depositing, patterning and etching thin films for silicon integrated circuit technology. Early applications of this technology include the digital mirror display [2] and the accelerometer [3]. The existence of accumulated design expertise, stable fabrication services, and electromechanical modeling tools has made the suspended-MEMS technology a good candidate for initial development of design and test tools for MEMS. Our synthesis approach [7][8] involves rapid translation of design specifications (such as the resonant frequency of a resonator) into a design that both functions as a resonator, and can meet the desired specifications. This design is then translated into layout using a parameterizable layout generator. This approach involves modeling the design problem as a formal numerical synthesis problem, and then solving it with powerful optimization techniques, a philosophy that has been successful in analog circuit synthesis. Although universal building blocks have not been discovered

for MEMS, components frequently used in system designs can be easily identified. In the suspended-MEMS area, reusable topologies include several kinds of accelerometers, gyroscopes, resonators, x-y positioners and micromirrors. Instead of redesigning these components each time a new system is proposed, engineers will benefit from synthesizer modules which tackle the routine design of frequently-used components.

Here, we combine our MEMS synthesis and contamination analysis capabilities into a synthesis-for-test environment as illustrated in Figure 1. A resonator design meeting a variety of specifications is synthesized. The susceptibility of this design to particulate contaminations is then determined. Design constraints derived from the particle-to-defect analysis are used in our synthesis process to minimize the misbehaviors resulting from spot contaminations. Re-synthesis of the same design using the derived constraints indicates that the number of catastrophic and parametric faults influenced by design rules can be reduced without sacrificing performance. A synthesis-for-test environment that avoids process simulation, mechanical finite element analysis (FEA), and solid modeling would be more efficient then the process illustrated in Figure 1. However, the non-existence of MEMS fault models currently prevents a more efficient approach from being realized.

We provide a brief background of the fabrication process and the device in Section 2, describe our synthesis approach in Section 3 and then describe the key concepts of our particle contamination analysis method in Section 4. Section 5 describes our experiments and results while Section 6 documents our conclusions.

2 BACKGROUND

The MUMPs technology chosen for our current synthesis work is well documented [9]. Microresonator structures are formed from a 2 μm-thick layer of polysilicon deposited over a 2 μm-thick sacrificial spacer layer of phosphosilicate glass (PSG). The PSG contact cuts act as mechanical anchor points that fix the microstructure to the substrate surface after the final HF release etch is completed.

A simplified layout of the microresonator is shown in Figure 2. This device has been well-researched and is commonly used for MEMS process characterization. The microresonator consists of a movable central shuttle mass which is suspended by folded-flexure springs on either side. The other ends of the folded-flexure springs are anchored to the lower layer. The microresonator can be thought of, as a spring-mass-damper system, the damping being provided by the air below and above the movable part. By applying a voltage across the fixed and movable comb fingers, an electrostatic force is produced which sets the mass into motion in the *x*-direction. The suspension is designed to be compliant in the *x* direction of motion and to be stiff in the

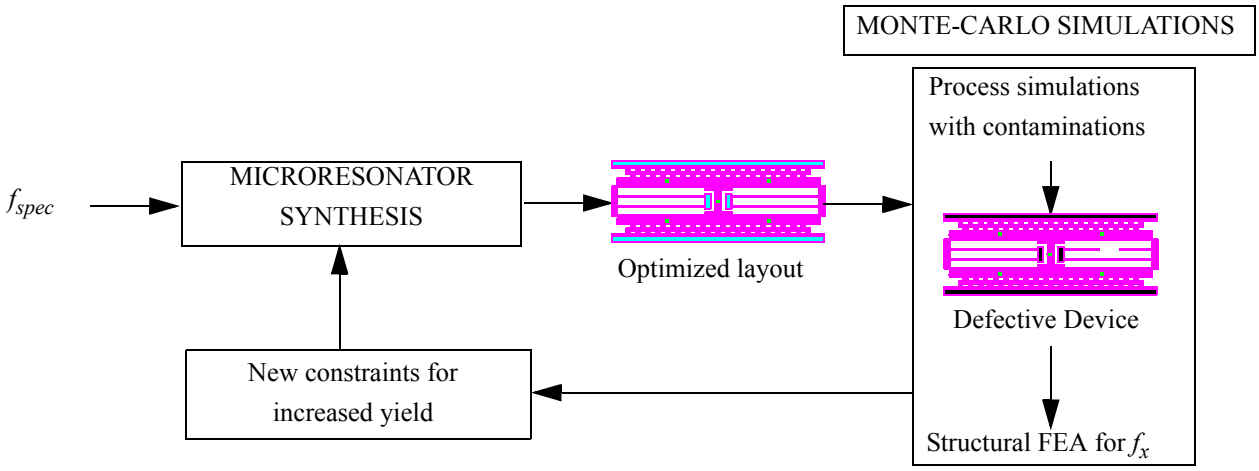

FIGURE 1. Overview of synthesis-for-test approach: Microresonators synthesized from input specifications are exposed to contaminations in different locations in the Monte-Carlo process simulations. This results in some of the devices being defective at the end of the process simulation. The resonant frequency of the defective structure is obtained using FEA and the deviations from designed performances are used to codify new constraints in the synthesis tool to reduce the effect of contaminations.

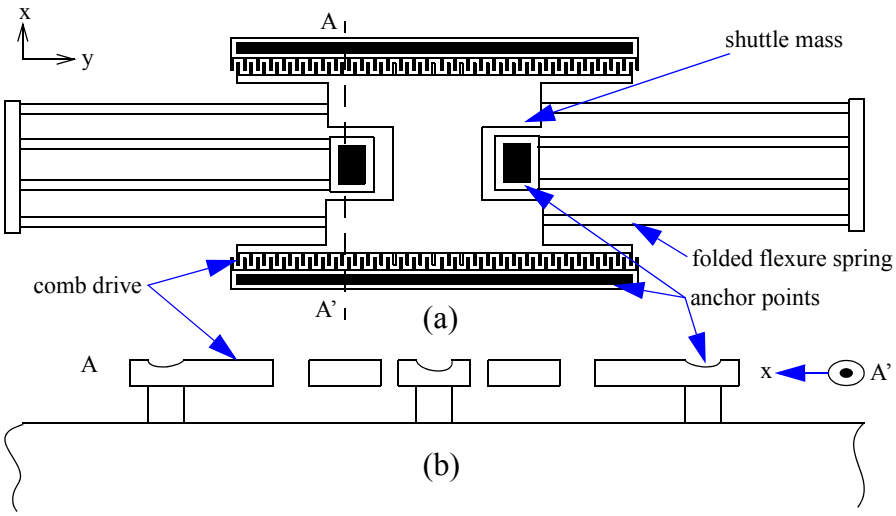

FIGURE 2. (a) Layout of the lateral folded-flexure comb-drive microresonator and (b) device cross-section A-A' in the MUMPS process.

orthogonal direction (y) to keep the comb fingers aligned. The microresonator has been used in building filters, oscillators [13] and in resonant positioning systems [14].

Surface-micromachined microstructures like the microresonator described above typically range from 0.1 to several μm in thickness and a few hundred μm to a mm in length. Typical space between structures ranges between 1 and 2 μm. The large surface area and small offset from adjacent surfaces make these microstructures vulnerable to stiction. Stiction is the adhesion of the microstructure to adjacent surfaces. It can occur during the final steps of the micromachining process (where the structure is released) or after packaging of the device due to out-of-range input signals or electromechanical instability [4]. Curling is another result of manufacturing conditions that causes structures of the micromechanical device to curl or buckle out of plane. Both stiction and curling cause MEMS misbehaviors and are therefore sources of yield loss during the fabrication of these devices.

Another cause of faulty behavior in MEMS is due to particulate contaminations that occur during and after fabrication [5]. Spot defects resulting from particulates can cause a significant perturbation in the structural and material properties of the microstructure [6]. Unlike failures due to stiction and curl, particulate failures can manifest sometime after manufacture and can therefore occur in the field. We use process simulations to predict the effects that contaminations have on the physical geometries and material properties of surface-micromachined components. Monte Carlo analysis using contamination data at every step of the manufacturing process is performed to produce a large spectrum of defective MEMS structures. Mechanical FEA of the structures are then performed to understand all the possible misbehaviors due to particulate contaminations.

3 RESONATOR SYNTHESIS

3.1 Design Variables and Models

Design variables of the microresonator include thirteen geometrical parameters of the shuttle mass, folded flexure, and comb drive elements, the comb-drive voltage and the number of fingers in the comb-drive are detailed in Figure 3 and listed in Table I. Additionally, geometric *style* variables, such as the width of the anchor supports, w_{ba} and w_{ca}, are necessary to completely define the layout, but do not affect the resonator behavior. Technology-driven design rules set minimum beam widths and minimum spaces between structures. Maximum beam lengths are constrained to 400 μm to avoid problems with undesirable curling due to stress gradients in the structural film and possible sticking and breakage during the wet release etch [16]. Maximum width of beams is constrained to 20 μm by the limited undercut of PSG to release the structures. The shuttle axle, the shuttle yoke and

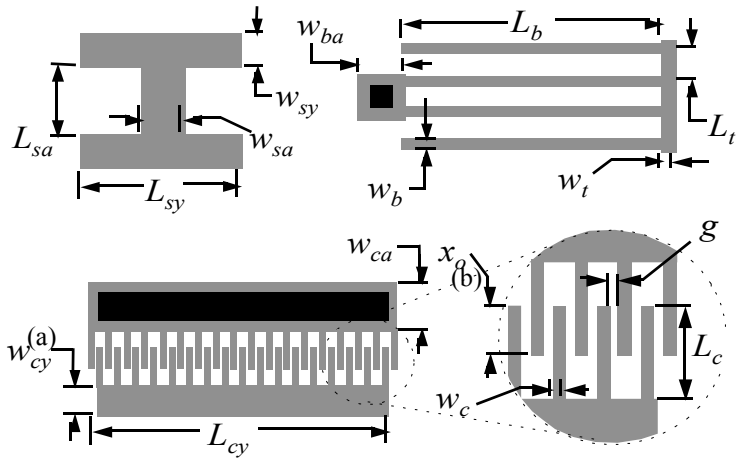

(c) (d)

FIGURE 3. Parameterized elements of the microresonator. (a) shuttle mass, (b) folded-flexure, (c) comb drive with *N* movable "rotor" fingers and (d) close-up view of comb fingers.

the comb yoke are at least 10 μm wide so that, they are relatively more rigid than folded-flexure beams. The comb yoke is allowed to extend up to 700 μm, to fill up the entire flexure length allowed for the resonator, even if the comb fingers occupy only a fraction of a length of the comb yoke.

The three rigid-body lateral translational and rotational modes (*x, y,* and *θ*) of the resonator are modeled by lumped mass-spring-damper equations of motion.The out-of-plane modes and other higher order modes can be controlled only by changing the thickness (*t*) of the structure. The thickness is fixed at 2 μm since the MUMPS process is being used and therefore, these modes are not constrained in this implementation.The effect of spring mass on resonance frequency is incorporated in effective masses for each lateral mode. The maximum velocity and total kinetic energy of the spring, from which the effective mass is extracted, is approximated from static mode shapes. Viscous damping generated by the moving shuttle in air is modeled as Couette flow using the equations in [10]. Damping factors of the other lateral modes do not enter into the design constraints and are

Table I: Design and style variables for the microresonator. Upper and lower bounds are in units of μm except *N* and *V*.

Design Variables							
Var.	**Description**	**Min**	**Max**	**Var.**	**Description**	**Min**	**Max**
L_b	length of flexure beam	2	400	w_{cy}	width of comb yoke	10	400
w_b	width of flexure beam	2	20	L_{cy}	length of comb yoke	2	700
L_t	length of truss beam	2	400	L_c	length of comb fingers	8	400
w_t	width of truss beam	2	20	w_c	width of comb fingers	2	20
L_{sy}	length of shuttle yoke	2	400	g	gap between comb fingers	2	20
w_{sy}	width of shuttle yoke	10	400	x_o	comb finger overlap	4	400
w_{sa}	width of shuttle axle	10	400				
N	number of rotor comb fingers	1	100	V	voltage amplitude	1 V	50V
Style Variables							
w_{ba}	width of beam anchors	11	11	w_{ca}	width of stator comb anchors	14	14

not calculated. Linear equations for the folded-flexure spring constants are found by using energy methods to find displacement for a unit load on the end of the spring [11]. Axial compression and extension are included in expressions for k_y and k_θ.

In the x-direction the spring constant [15] and the effective mass are:

$$k_x = \frac{2Etw_b^3}{L_b^3} \quad \frac{L_t^2 + 14\alpha L_t L_b + 36\alpha^2 L_b^2}{4L_t^2 + 41\alpha L_t L_b + 36\alpha^2 L_b^2} \tag{1}$$

where E is the Young's modulus of polysilicon, t is the polysilicon thickness, and $\alpha = (w_t/w_b)^3$

$$m_x = m_{shuttle} + m_{t,\,eff} + m_{b,\,eff} \tag{2}$$

$$m_{b,\,eff} = \frac{m_{beams}}{140} \quad \frac{832L_t^4 + 16121\alpha L_t^3 L_b + 92706\alpha^2 L_t^2 L_b^2 + 138348\alpha^3 L_t L_b^3 + 62208\alpha^4 L_b^4}{(4L_t^2 + 41\alpha L_t L_b + 36\alpha^2 L_b^2)^2} \tag{3}$$

$$m_{t,\,eff} = \frac{m_{truss}}{280} \quad (57L_t^6 + 1020\alpha L_t^5 L_b + 4644\alpha^2 L_t^4 L_b^2 + 1120L_t^4 L_b^2 + 17920\alpha L_t^3 L_b^3 + 91840\alpha^2 L_t^2 L_b^4 + 161280\alpha^3 L_t L_b^5 + 90720\alpha^4 L_b^6)/[L_b^2(4L_t^2 + 41\alpha L_t L_b + 36\alpha^2 L_b^2)^2] \tag{4}$$

where $m_{shuttle}$ is the shuttle mass, $m_{t,eff}$ is the effective mass of all truss sections, $m_{b,eff}$ is the effective mass of all the long beams, m_{truss} is the total mass of all truss sections, and m_{beams} is the total mass of all the long beams.

General analytic equations for the lateral comb-drive force, F_x, as a function of w_c, g, structure thickness, and sacrificial spacer thickness are derived in [12]. For the special case of equal comb finger width, gap, thickness, and spacing above the substrate ($w_c = g = t = d$), each comb drive generates a force that is proportional to the square of the voltage, V, applied across the comb fingers.

$$F_x \cong 1.12\varepsilon_o N \frac{t}{g} V^2 \tag{5}$$

where ε_o is the permittivity of air, N is the number of fingers in the movable comb drive, and V is the instantaneous voltage applied across the comb drive.

3.2 Design Constraints

The design constraints can be classified into two categories: geometrical constraints which are directly related to the physical dimensions of the microresonator and functional constraints which are related to the behavior of the microresonator. The geometric constraints illustrated in Figure 4 are necessary to ensure a functional resonator.

A summary of the functional constraints on the design specifications is given in Table II. An essential specification is resonant frequency of the lowest (preferred) mode, $\omega_x = 2\pi f_x = \sqrt{k_x/m_x}$, where k_x is the spring constant and m_x is the effective mass. A valid layout must have a resonant frequency within 1% of the specified value.

Assuming the system is underdamped, the displacement amplitude at resonance is $x_{disp} = QF_x/k_x$, where $F_x \propto NV^2$ is the comb-drive force, $Q = \sqrt{m_x k_x / B_x^2}$ is the quality factor, and B_x is the damping coefficient. We have constrained $x_{max} > 2$ μm at a drive voltage of $V < 50$ V to enable easy visual confirmation of resonance, and $Q \geq 5$ to ensure underdamped resonant operation.

For stability, the restoring force of the spring in the y direction must be much greater than the destabilizing electrostatic force from the comb drive (*i.e.,* $3k_{e,y} < k_y$). A similar stability constraint must hold for the rotational mode. Resonant frequencies of the other two lateral modes, f_y and f_θ, must be at least three times greater than f_x to decouple the modes adequately.

The two accuracy constraints in Table II are required to prevent the optimization search from venturing into those parts of the design space where the models used are not accurate. The buckling constraint ensures that the beams are not so long that

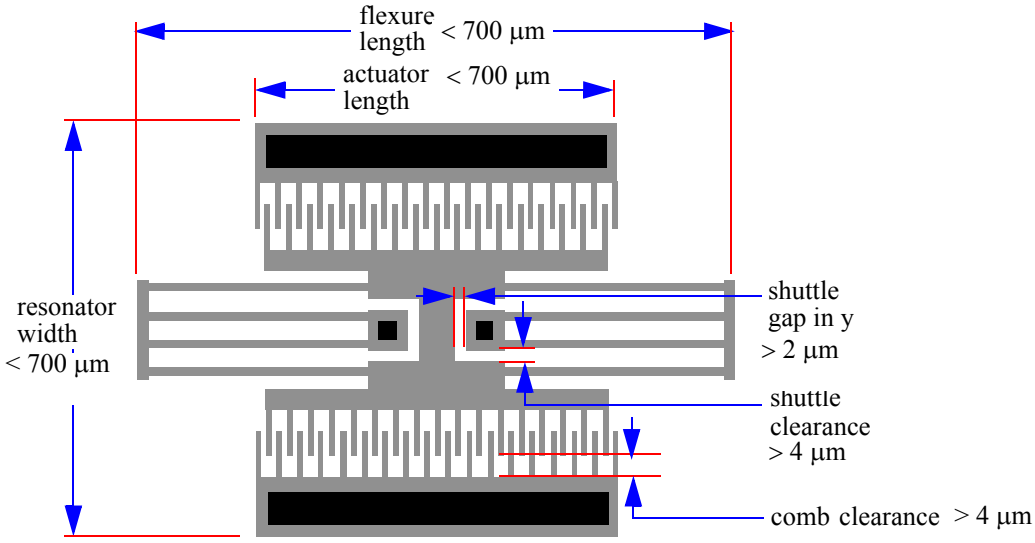

FIGURE 4. Geometric constraints: These constraints limit the overall size of the microresonator and also prevent the moving parts from colliding into the fixed parts of the microresonator.

they buckle due to residual stress due to the fabrication process.

Table II: Functional constraints of resonator synthesis.

Constraint Description	Expression	MIN	MAX
resonant frequency	$\frac{f_x}{f_{spec}}$	0.99	1.01
stroke at resonance	x_{disp}	2 µm	100 µm
quality factor in x	Q	5	10^5
y-axis stability	$\frac{k_{e,y}}{k_y}$	0	1/3
θ stability	$\frac{k_{e,\theta}}{k_\theta}$	0	1/3
in-plane mode separation	$\frac{f_x}{f_{in-plane}}$	0	1/3
k_y accuracy	$\frac{k_y}{k_{y,axle}}$	0	1/10
k_x accuracy	$\frac{x_{disp}}{L_b}$	0	1/10
buckling	$\frac{L_b}{L_{cr}}$	0	1/2

3.3 Synthesis Algorithm

Our synthesis approach is to select the design that minimizes an objective function and therefore, may be considered optimal. The synthesized result depends very strongly on the choice of objective function. The synthesis problem is translated into a constrained optimization formulation that is solved using a non-linear constrained optimization technique. During the optimization, designs are evaluated by the values of the constraint functions and the objective functions for the current values of the

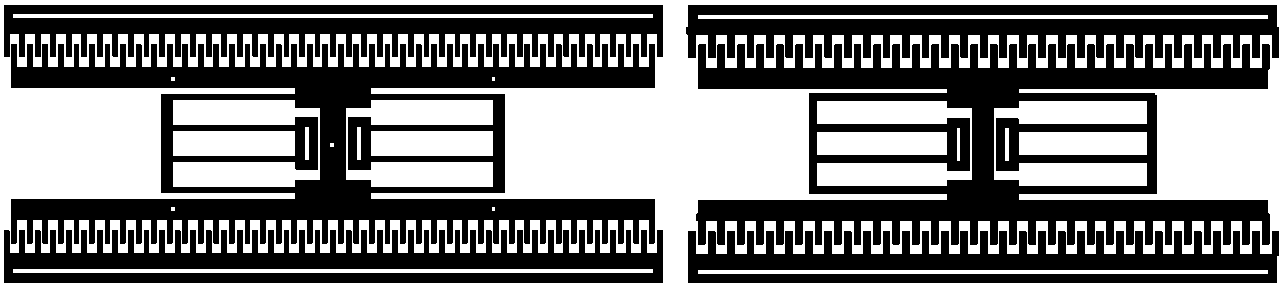

FIGURE 5. 100 kHz microresonator synthesized with (a) minimum MUMPS design rules (b) minimum MUMPS rules + DFT (Design For Testability) extensions from contamination analysis.

design variables. Depending on the choice of the objective function, there can be more than one minimum point in the optimization, due to the complex non-linear characteristics of the individual equations in the lumped-element models. Furthermore, since our goal is synthesis, we need to be independent of any choice of starting point for the optimization.

In order to increase the probability of finding a better design (i.e., move closer to the global optimum) a gridded multi-start algorithm coupled with a gradient-based constrained optimization efficiently solves for the global minimum of the objective function. The non-linear constrained optimization formulation can be written as:

$$\begin{aligned} min_{\underline{u}} \quad & z = \sum_{i=1}^{\wedge} w_i \cdot f_i(\underline{u}) \\ \text{s.t.} \quad & \underline{h}(\underline{u}) = 0 \\ & \underline{g}(\underline{u}) \le 0 \\ & u \in U_P \end{aligned}$$

where $\underline{u}$ is the vector of independent design variables given in Table I; $\underline{f}(\underline{u})$ is a set of objective functions that codify performance specifications the designer wishes to optimize, *e.g.*, area; $\underline{h}(\underline{u}) = 0$ and $\underline{g}(\underline{u}) \le 0$ are each a set of functions that implement the geometric and functional constraints. Scalar weights, w_i, balance competing objectives. The decision variables can be described as a set $\underline{u} \in U_P$, where U_P is the set of allowable values for $\underline{u}$ (described by the bounds in Table I).

4 CONTAMINATION ANALYSIS

We have developed a process/contamination simulator tool called CARAMEL (**C**ontamination **A**nd **R**eliability **A**nalysis of **M**icro**E**lectromechanical **L**ayout) for analyzing the impact of particulates on the geometrical and material properties of microelectromechanical layout [6]. CARAMEL requires three inputs:

- **Design definition:** This is typically a layout of the design in the Caltech Intermediate Form (CIF).
- **Process definition:** This includes a sequence of process steps with all the required details such as deposition thickness, etching rate, etching time, *etc.*
- **Contamination definition:** This includes geometrical and material characteristics of the particulate, its location in the MEMS layout, and the process step of introduction.

CARAMEL performs process simulation and creates a three-dimensional representation of the defective microelectromechanical structure. It then extracts a mesh representation from the defective structure whose form is completely compatible with low-level FEA tools such as ABAQUS [17]. Eigenmode analysis of the finite-element model then allows us to link the contamination of concern to a defective structure and a faulty behavior. Resonant frequency (in the *x*-direction) is analyzed because it is one of the crucial parameters for determining if the resonator is functioning properly [3]. Defective structures can then be classified based on their corresponding misbehaviors. Monte Carlo iteration in the flow of Figure 1 provides a mechanism for

Particle location	Diameter size (μm)	Added after process step #	Resonant frequency f_x (kHz)	Percentage change in f_x (%)
NONE	-	-	69.7	-
comb	2.4	Poly1 deposition	90	+29
beam	1.5	PSG deposition	68.6	-1.6
shuttle	1.5	PSG depositing	70	≈0

Table III:Three representative cases of particle analysis using CARAMEL.

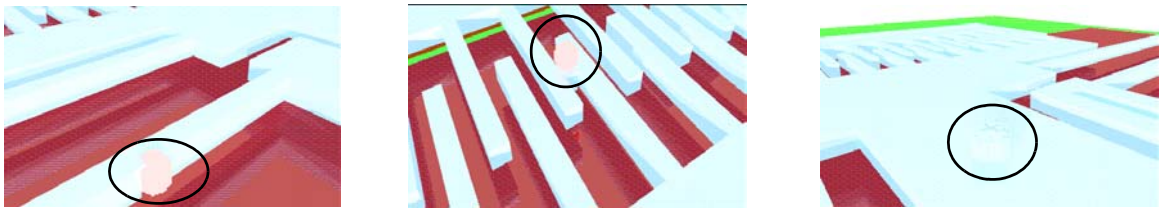

(a) (b) (c)

FIGURE 6. Three-dimensional representations of a defective resonators for a contamination particle located (a) on a flexure beam, (b) between adjacent comb fingers, and (c) on the shuttle mass.

creating realistic fault models for MEMS primitive elements at the next level of abstraction.

InTable III, we provide details of three representative cases of particle analysis using CARAMEL. The first entry of Table III gives the resonant frequency for a defect-free resonator. The impact of all three particles on the structure of the resonator is shown in Figure 6, while the corresponding misbehaviors (impact on resonant frequency) reported by ABAQUS are shown in Table III. Details for each particle are given below:

- **Beam:** The impact of a particle affecting a beam of the folded-flexure is illustrated in Figure 6b. Such a contamination results in a slightly heavier beam. The small increase in mass of the beam reduces the resonant frequency by only 1.61%. Note, the long-term reliability of this defect may be greatly degraded but cannot be predicted using FEA.
- **Comb:** Figure 6b shows the impact of a contamination located between adjacent comb fingers. The process simulation phase of CARAMEL reveals that the contamination welds together the two normally-moving fingers. The welded fingers transforms the corresponding comb drive into a single structure. The result obtained from FEA shows a 29% increase in resonant frequency; an indication that this defect has caused a catastrophic failure.
- **Shuttle:** Figure 6c shows another interesting case where the particle becomes totally encapsulated by the shuttle mass. Process simulation by CARAMEL indicates that a bump is formed on the shuttle surface. The creation of such a bump slightly increases the mass of the shuttle. However, FEA reveals that resonant frequency is virtually unaffected.

5 SIMULATION EXPERIMENTS

First, we synthesize a 100 kHz resonator with the objective that area and applied voltage be minimized. The resulting design is then subjected to a particle contamination analysis to determine its susceptibility to spot defects. The results of the contamination analysis are then analyzed to derive new synthesis constraints in order to reduce the misbehaviors resulting from particles. The 100kHz resonator is then re-synthesized using the new synthesis constraints. Finally, contamination analysis is performed on the new design to determine its new level of robustness.

The contamination simulation experiments involve the variation of the following three parameters of the defects: size, location and process step of introduction. All of these parameters are varied simultaneously and randomly. The nature of each parameter is explained below:

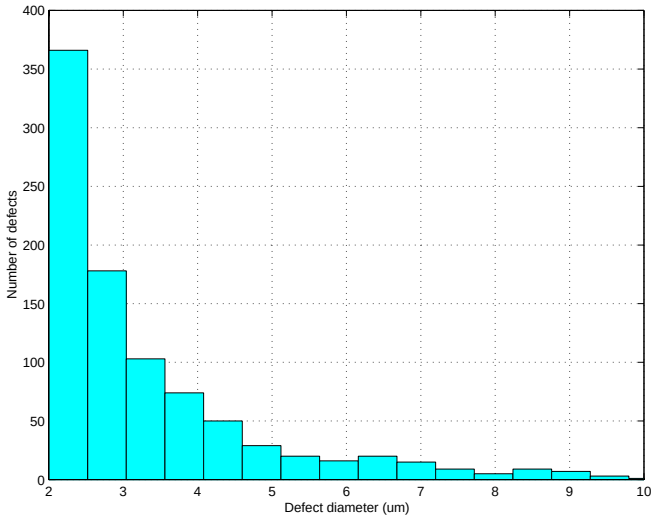

FIGURE 7. Histogram showing defect size distribution. About 75% of the defects are less than 4 μm in diameter.

- **Defect size distribution:** The defect size is distributed exponentially and is shown in the histogram of Figure 7.
- **Defect location distribution:** The defect location PDF (probability distribution function) is uniform and covers the whole area of the resonator as defined by its bounding box. The defect density per unit area and per process step is kept constant for all experiments.
- **Process step of introduction:** Contaminations are randomly introduced into every process step. However, only a subset of the process steps lead to defects that affect the structure after fabrication. In all other steps the contaminants are etched away without any lasting effects.

The required number of defect simulation runs for the two resonators (synthesized without design-for-testability (DFT) and with DFT-based design constraints) is made proportional to the bounding box area of the respective layout. This makes sense as a resonator with larger area will have more defects (not all would affect the actual body of the resonator though) than one with a smaller bounding box area given the condition that the defect density is a constant. Design characteristics and the results of the defect simulation, as done by extracting the fundamental resonant frequency f_x by the FEA tool ABAQUS, for the resonator designs without and with DFT changes are included in Tables IV and V, respectively. All ABAQUS simulations are 3-dimensional and no constraints are placed on the six degrees of motion.

In Table IV, the *anchor* defects are those which either bridge the mobile structure (shuttle or beams) to the substrate. The *finger* defects are those which connect a movable finger (a finger connected to the shuttle) and an anchored finger. (See Figure 6b for an example.) Such defects greatly restrict resonator motion. *Beam* defects affect the truss and flexure beams of the resonator. Localization of the defects is important for understanding which defects can be affected by the alteration of design. Because the spacing between the substrate and the movable structure is fixed by the process, defects that cause extra, unwanted anchors can only be alleviated by reducing the area of the movable structure. However, the effect of both the finger and beam defects can be adjusted by varying the design rules.

Analyzing the results of Table IV lead to the following observations:

- Finger and flexure-beam defects together constitute about 25% of the catastrophic defects.
- In this class of defects (beam and inter-finger) the inter-finger defects constitute the major share.

The choice of new synthesis constraints is made through an analysis of the defect size distribution. The histogram of Figure 7 shows that out of a total of 944 defects:

- 540 have a diameter d such that $2\mu m \leq d < 3\mu m$
- 180 have a diameter d such that $3\mu m \leq d \leq 4\mu m$

So 75% of the defects have a diameter of less than 4μm and 57% have $d < 3\mu m$. Based on this observation, we propose new synthesis constraints that require finger gap to change from 2μm to 3μm. The characteristics of the new design synthesized using these constraints are given in Table V.

Table IV: 100KHz resonator design without design-for-testability constraints.

Parameters of resonator	Area of Bounding box = 47996 μm^2 Finger width = 2.0 μm Finger gap = 2.0 um Operating voltage = 28.2 volts No. of fingers = 42 Max. displacement = 2.0 μm	
Number of process simulations	454	
Total number of defects	95 (20.93% of total)	
Fault classification	**Fault class**	**No. of instances**
	Harmless ($\Delta f_x < 5\%$)	50
	Parametric ($5\% < \Delta f_x < 30\%$)	3
	Catastrophic ($\Delta f_x > 30\%$)	42
Catastrophic distribution	**Fault location**	**No. of instances**
	Anchor	31
	Finger	9
	Beam	2

Table V: 100KHz resonator design with design-for-testability constraints.

Parameters of resonator	Area of Bounding box = 42884 μm^2 Finger width = 2.0 μm Finger gap = 3.0 μm Operating voltage = 36.8 volts No. of fingers = 30 Max. displacement = 2.0 μm	
Number of process simulations	406	
Total number of defects	77 (18.97% of total)	
Fault classification	**Fault class**	**No. of instances**
	Harmless ($\Delta f_x < 5\%$)	42
	Parametric ($5\% < \Delta f_x < 30\%$)	4
	Catastrophic ($\Delta f_x > 30\%$)	31
Catastrophic distribution	**Fault location**	**No. of instances**
	Anchor	24
	Finger	4
	Beam	3

The results of Tables V and VI lead to the following observations.

- The application of DFT has reduced the total number of catastrophic defects by about 25%.
- Among the catastrophic defects, the contribution of the finger defects has decreased from 21%

(without DFT) to 13% (with DFT) showing clearly that wider finger gap has reduced the catastrophic defects caused by bridging between fixed and mobile fingers. Naturally, the combined contribution of inter-finger and beam defects has decreased from about 26% (without DFT) to 22% (with DFT) while that of anchor defects has gone up from 74% (without DFT) to 78% (with DFT). This is due to the fact that the thickness of the ANCHOR1 layer is unaffected by any design parameter change.

- The 25% reduction in catastrophic failures is also accompanied by a 10.6% decrease in bounding box area and a 30% increase in operating voltage while the specifications of the resonator (maximum displacement and resonant frequency) are maintained.
- The effect of the decrease in area is shown by the relative number of defects affecting the structure (20.93% for no DFT and 18.97% with DFT), which drop by about 10%, as is expected. This figure is only approximate as the real figure will depend on the *effective area* of the layout.

6 CONCLUSIONS

We have shown the applicability of DFT for improving the yield of MEMS devices like the microresonator. Utilizing new design constraints derived from contamination analysis has reduced the number of catastrophic failures by 25% for a given design at the cost of increased operating voltage but not at the cost of more area. In fact, there was a reduction in area due to DFT, which indicates that there is the possibility of reducing the voltage cost and/or catastrophic defects by sacrificing the reduction in area. However, the maximum displacement and the resonant frequency specifications of the original design are preserved.The derived set of new design rules are rather *ad hoc* and represent a simplistic attempt to show that it is possible to improve robustness through design. The considerations of other design rules for a variety of designs will most likely lead to an optimization of the DFT constraints. But this process is currently CPU intensive in that more than 40 hours of CPU time are required to conduct a Monte-Carlo contamination analysis of a single design. A synthesis-for-test environment that utilizes effective fault models, and thus avoids process simulation, mechanical FEA, and solid modeling would be much more effective in generating better DFT constraints.

7 REFERENCES

[1] W. C. Tang, T.-C. H. Nguyen, M. W. Judy, and R. T. Howe, “Electrostatic Comb Drive of Lateral Polysilicon Resonators,” *Sensors and Actuators A*, 21 (1990) 328-31.

[2] L. J. Hornbeck, “Current Status of the Digital Micromirror Device (DMD) for Projection Television Application,” *Proc. of International Electron Devices Meeting*, Washington, D.C., 1993.

[3] R. S. Payne, S. Sherman, S. Lewis and R.T. Howe, “Surface Micromachining: From Vision to Reality to Vision (accelerometer),” *Proc. of International Solid State Circuits Conference*, pp. 164-165, San Francisco, CA, 1995.

[4] R. Maboudian and R.T. Howe, “Critical Review: Stiction in Surface Micromechanical Structures,” *Journal of Vacuum Science and Technology B (Microelectronics and Nanometer Structures)*, Vol. 15, No. 1, pp. 1-20, Jan. 1997.

[5] A. Kolpekwar, R. D. Blanton and D. Woodilla, “Failure Modes for Stiction in Surface-Micromachined MEMS,” *Proc. 1998 International Test Conference*, Oct. 1998.

[6] A. Kolpekwar, C. Kellen and R. D. Blanton “MEMS Fault Model Generation using CARAMEL,” *Proc. of International Test Conference*, Oct. 1998.

[7] T. Mukherjee, S. Iyer and G. K. Fedder, “Optimization-based Synthesis of Microresonators,” *Sensors and Actuators A*, 70, (1998) 118-127.

[8] T. Mukherjee and G. K. Fedder. “Structured Design of Microelectromechanical Systems,” In Design Automation Conference, pp. 680-685, June 1997.

[9] D. A. Koester, R. Mahadevan, K. W. Markus, *MUMPs Introduction and Design Rules*, MCNC MEMS Technology Applications Center, 3021 Cornwallis Road, Research Triangle Park, NC 27709, Rev. 3, Oct. 1994.

[10] X. Zhang and W. C. Tang, *Sensors and Materials*, Vol. 7, No. 6, pp.415-430, 1995.

[11] J. M. Gere and S. P. Timoshenko, *Mechanics of Materials,* 4th ed., Boston: PWS Publishing Co., 1997.

[12] W. A. Johnson and L. K. Warne, *J. of Microelectromechanical Systems*, Vol.4, No. 1, pp.49-59, 1995.

[13] C. T.-C. Nguyen and R. T. Howe, "Micromechanical resonators for frequency references and signal processing," *Proc. IEEE Int. Electron Devices Meeting*, San Francisco, CA, 1994, pp. 343.

[14] M.-H. Kiang, O. Salgaard, K. Y. Lau and R. S. Muller, "Electrostatic Combdrive-Actuated Micromirrors for Laser-Beam Scanning and Positioning", *J. of Microelectromechanical Systems*, Vol. 7, No. 1, March 1998, pp. 27-37.

[15] G. K. Fedder, *Simulation of Microelectromechanical Systems*, Ph.D. thesis, University of California at Berkeley, Sept. 1994.

[16] C. H. Mastrangelo and C. H. Hsu, "A Simple Experimental Technique for the Measurement of the Work of Adhesion of Microstructures", *Technical Digest, IEEE Solid-State Sensor and Actuator Workshop*, Hilton Head Island, South Carolina, June 1992, pp. 208-212.

[17] Hibbit, Karlsson and Sorensen, Inc., "ABAQUS User Manual", Vol. 2, Pawtucket RI, 1995.